Reduction of the Effect of Machine Saturation on the Quality of Self-Sensing Control

Niklas Himker, *Member, IEEE*, Pieris Sourkounis, Viktor Willich, *Graduate Student Member, IEEE*, Georg Lindemann, and Axel Mertens, *Senior Member, IEEE*

***Abstract*—Saturation effects are one of the main challenges arising in rotor position estimation for a permanent magnet synchronous machine (PMSM). In this article, a method to cope with saturation effects for self-sensing control (SSC) of PMSMs is derived analytically. The applied SSC algorithm is based on a numerical optimization of a residual, which includes the inductance matrix of the machine. By taking the cross-coupling between the d- and q-axis into account, not only is the estimation error minimized, but also the application of SSC is enabled at heavily saturated operating points. This is achieved by using the additional information provided by the mutual inductance, which is used to model the cross-coupling. Furthermore, harmonic estimation errors caused by saturation effects are eliminated by applying a simplified analytical model of the harmonic components to the inductance matrix. With these approaches, the effects of saturation on the quality of the SSC are significantly reduced. Since both of these methods rely on exact knowledge of the machine's inductances, a technique to determine these is provided. All results are validated experimentally.**

***Index Terms*—Cross-coupling, multiple saliencies, mutual inductance, numerical optimization, self-sensing control (SSC).**

I. Introduction

WHILE the use of an encoder for a field-oriented control (FOC) is and has generally been the standard approach, there is a long history of using self-sensing control (SSC) for permanent magnet synchronous machines (PMSMs) [1], [2]. The ambition to run a PMSM with SSC promises a reduction of the overall cost and size of the drive, or alternatively, the option to ensure safe operation of the system if an encoder fails [3].

The research in this field has resulted in two different approaches. The first is the evaluation of the back-electromotive force (EMF), which utilizes the direct relationship between the rotational speed of the machine and the induced voltage due to the EMF. But since this method is only applicable at medium and high speeds [4], a second approach which is based on the inherent anisotropy of the inductance matrix of a PMSM has been developed [1]. Rotor-fixed variations of the magnetic reluctance introduce the anisotropic behavior of the rotor, which is a second-order harmonic of the stator inductance dependency on the rotor position and makes anisotropy-based position estimation possible at low speed and at standstill [1]. These anisotropy-based SSC schemes rely on an excitation with a high-frequency (HF) signal [5]. In this article, the voltage signal is a square-wave injection (SWI), which is injected with pulsewidth modulation (PWM) frequency [6].

The beneficial behavior of the rotor-fixed variations of the stator inductance is superimposed by saturation. The saturation introduces effects that impact the SSC capabilities negatively, if they are not compensated for. These are namely the cross-coupling effect, modeled via a mutual inductance [7], and multiple saliencies [8], [9]. These negative effects and a possibility to compensate for them constitute the main topic of this article.

A mutual inductance will, if not considered properly, introduce an estimation error of the rotor position [10]. The coupling of the d- and q-axis leads to a current response in the q-axis when the d-axis is excited via a voltage signal, which can be misinterpreted and results in a falsely estimated rotor position. This characteristic is well known, and leads to a constant component of the estimation error [11], [12].

If the mutual inductance and the self-inductances are known, the compensation can be achieved by adding the calculated value of the estimation error to the initially estimated rotor angle [13]. In [14], [15], and [16], an additional reference frame for the rotor position estimator is introduced. The mutual inductance basically introduces a rotation of the second-order harmonic of the rotor-fixed saliency. Thus, the minimum of inductance (usually oriented on the d-axis) is rotated by a certain angle. The additional reference frame is always oriented in the direction of the minimum of inductance. This results in the inductance matrix being diagonalized, i.e., there are only self-inductances and no mutual inductance in the additional reference frame. For this approach, the injected signal and current are also oriented in the d-axis of the additional reference frame [16].

In the method proposed in this article, the position of the rotor is estimated based on the current response to the HF voltage signal using numerical optimization [17]. An estimator that accounts for the mutual inductance in the residual, which is minimized by the numerical optimization, is investigated with a special focus on the information provided by the mutual inductance. This approach allows the mutual inductance to be

Received 15 May 2024; revised 3 August 2024 and 26 September 2024; accepted 23 October 2024. Date of publication 28 October 2024; date of current version 18 December 2024. This work was supported by the Deutsche Forschungsgemeinschaft (DFG, German Research Foundation)—Project Identification No. 329209868. Recommended for publication by Associate Editor W. Xu. *(Corresponding author: Niklas Himker.)*

Niklas Himker, Pieris Sourkounis, Viktor Willich, and Axel Mertens are with the Institute for Drive Systems and Power Electronics, Leibniz University Hannover, 30167 Hannover, Germany (e-mail: niklas.himker@ial.uni-hannover.de).

Georg Lindemann is with the CARIAD SE, 38442 Wolfsburg, Germany.

Color versions of one or more figures in this article are available at https://doi.org/10.1109/TPEL.2024.3487314.

Digital Object Identifier 10.1109/TPEL.2024.3487314

used for position estimation when the self-inductances in both axes are equal due to saturation [18].

While the second-order saliency is exploited to estimate the rotor position, higher order saliencies translate into a harmonic variation of the inductances with the rotor position. The resulting discrepancy between the actual and assumed inductances leads to an oscillating error in the estimation when the machine is rotating.

There are some heuristic techniques, which can be used to reduce this harmonic error. In [8] and [16], the current response of the injected voltage signal is measured while using an encoder, thus resulting in a measurement that only contains the mismatch between the system and the applied model, since the position error is always zero due to the encoder. By subtracting this measured signal from the current response in SSC operation, these unconsidered effects are compensated for. Alternatively, resonant filter structures can be used to reduce the harmonic error in steady-state operation [19].

In this article, an analytical model for multiple saliencies and their effect on the inductances is proposed. Based on this modeling, the inductance values used in the rotor position estimation are adjusted as a function of the estimated rotor position. In this way, saliency of higher order is anticipated in the model and in the residual. As a result, the rotor position estimate remains error free. This eliminates all effects on the rotor position estimation error that occur due to saturation of the PMSM, which corresponds to the main contribution of this work.

To use both the mutual inductance and the multiple anisotropy in the rotor position estimation, it is essential to identify the rotor-dependent inductance matrix. In this article, a method for the determination of the inductance matrix is presented. The method uses the residual of the numerical optimization for SSC and a position sensor.

In the following Section II, the utilized model of the PMSM and SSC scheme is introduced, along with a description of the test bench used. Section III deals with the determination technique for the inductance matrix. The effects introduced by the mutual inductance and its compensation are analyzed in Section IV. In Section V, a method to suppress harmonic estimation errors due to multiple saliencies is provided. The two methods are validated in the corresponding sections. Finally, Section VI concludes this article.

II. Fundamentals

In the following, the model of the PMSM and the adaptation law of the SSC with numerical optimization are presented.

A. Model of the PMSM With a Mutual Inductance and a Higher Order Saliency

The model of the PMSM is based on the stator voltage ${}^{(\alpha\beta)}v$ in the $\alpha\beta$-reference frame. The ohmic voltage drop and the law of induction lead to

$$(\alpha\beta)_{\vec{v}} = R\,{}^{(\alpha\beta)}\vec{i} + \frac{\mathrm{d}}{\mathrm{d}t}\,{}^{(\alpha\beta)}\vec{\Psi} \quad . \tag{1}$$

The stator resistance R is assumed to be isotropic. The current in the $\alpha\beta$-reference frame is ${}^{(\alpha\beta)}\vec{i}$ and the flux linkage of the stator is ${}^{(\alpha\beta)}\vec{\Psi}$. The flux linkage from the dq-reference frame is transformed by

$$\frac{\mathrm{d}}{\mathrm{d}t}\,{}^{(\alpha\beta)}\vec{\Psi} = \frac{\mathrm{d}}{\mathrm{d}t}\,{}^{(\alpha\beta)}\mathbf{T}_{(\mathrm{dq})}\,{}^{(\mathrm{dq})}\vec{\Psi} \tag{2}$$

with

$${}^{(\alpha\beta)}\mathbf{T}_{(\mathrm{dq})} = \begin{pmatrix} \cos(\gamma_{\mathrm{el}}) & -\sin(\gamma_{\mathrm{el}}) \\ \sin(\gamma_{\mathrm{el}}) & \cos(\gamma_{\mathrm{el}}) \end{pmatrix} \tag{3}$$

into the stator-fixed reference frame. Since the transformation matrix ${}^{(\alpha\beta)}\mathbf{T}_{(\mathrm{dq})}$ (by using the rotor position γ_{el}) and the flux linkage ${}^{(\mathrm{dq})}\vec{\Psi}$ are dependent on time, the product rule is used for derivation. This results in

$$\frac{\mathrm{d}}{\mathrm{d}t}\,{}^{(\alpha\beta)}\vec{\Psi} = {}^{(\alpha\beta)}\mathbf{T}_{(\mathrm{dq})}\frac{\mathrm{d}}{\mathrm{d}t}\left({}^{(\mathrm{dq})}\vec{\Psi}\right) + \frac{\mathrm{d}}{\mathrm{d}t}\left({}^{(\alpha\beta)}\mathbf{T}_{(\mathrm{dq})}\right){}^{(\mathrm{dq})}\vec{\Psi} \quad . \tag{4}$$

The voltage differential equation of the stator is transformed into the dq-reference frame, yielding

$$\begin{aligned} {}^{(\mathrm{dq})}\vec{v} &= {}^{(\mathrm{dq})}\mathbf{T}_{(\alpha\beta)}R\,{}^{(\alpha\beta)}\vec{i} + {}^{(\mathrm{dq})}\mathbf{T}_{(\alpha\beta)}\frac{\mathrm{d}}{\mathrm{d}t}\,{}^{(\alpha\beta)}\vec{\Psi} \\ &= R\,{}^{(\mathrm{dq})}\vec{i} + \frac{\mathrm{d}}{\mathrm{d}t}\left({}^{(\mathrm{dq})}\vec{\Psi}\right) + {}^{(\mathrm{dq})}\mathbf{T}_{(\alpha\beta)}\frac{\mathrm{d}}{\mathrm{d}t}\left({}^{(\alpha\beta)}\mathbf{T}_{(\mathrm{dq})}\right){}^{(\mathrm{dq})}\vec{\Psi} \\ &= R\,{}^{(\mathrm{dq})}\vec{i} + \frac{\mathrm{d}}{\mathrm{d}t}\left({}^{(\mathrm{dq})}\vec{\Psi}\right) + \mathbf{J}\omega_{\mathrm{el}}\,{}^{(\mathrm{dq})}\vec{\Psi} \end{aligned} \tag{5}$$

with

$$\omega_{\mathrm{el}} = \frac{\mathrm{d}}{\mathrm{d}t}\gamma_{\mathrm{el}} \quad \text{and} \quad \mathbf{J} = \begin{pmatrix} 0 & -1 \\ 1 & 0 \end{pmatrix} \quad . \tag{6}$$

The flux linkage of the PMSM depends on both the permanent magnet and the current, and can be represented in the sum as

$${}^{(\mathrm{dq})}\vec{\Psi} = {}^{(\mathrm{dq})}\vec{\Psi}_{\mathrm{L}} + {}^{(\mathrm{dq})}\vec{\Psi}_{\mathrm{PM}} \quad . \tag{7}$$

The flux linkage ${}^{(\mathrm{dq})}\vec{\Psi}_{\mathrm{PM}}$ indicates the part that is contributed by the permanent magnet. The other part ${}^{(\mathrm{dq})}\vec{\Psi}_{\mathrm{L}}$ is contributed by the stator current. This is set up with

$${}^{(\mathrm{dq})}\vec{\Psi}_{\mathrm{L}} = \mathbf{L}_{(\mathrm{dq})}\left({}^{(\mathrm{dq})}\vec{i}\right){}^{(\mathrm{dq})}\vec{i} \tag{8}$$

by using the secant inductance. The secant inductance

$$\begin{aligned} \mathbf{L}_{(\mathrm{dq})} = &\begin{pmatrix} L_{\mathrm{d},0} & L_{\mathrm{dq},0} \\ L_{\mathrm{dq},0} & L_{\mathrm{q},0} \end{pmatrix} \\ &+ \begin{pmatrix} L_{\mathrm{d},6}\cos\left(6\gamma_{\mathrm{el}} + \varphi_{\mathrm{d},6}\right) & L_{\mathrm{dq},6}\cos\left(6\gamma_{\mathrm{el}} + \varphi_{\mathrm{dq},6}\right) \\ L_{\mathrm{dq},6}\cos\left(6\gamma_{\mathrm{el}} + \varphi_{\mathrm{dq},6}\right) & L_{\mathrm{q},6}\cos\left(6\gamma_{\mathrm{el}} + \varphi_{\mathrm{q},6}\right) \end{pmatrix} \end{aligned} \tag{9}$$

is used [20]. The index d or q is used for the respective self-inductances. The mutual inductance (also known as the cross-coupling inductance) is indicated by the index dq and is assumed to be identical for the entries of the secondary diagonal. The dependence on the rotor position is represented by a sum in which a linear superposition is assumed [20]. In this article, only the sixth harmonic of the inductance is considered, as this

is the most significant harmonic of the device under test. The index 0 is used for the direct component of the inductances and the index 6 is used for the harmonic of the inductance. The harmonic functions of the inductances are assigned with an angle φ and a corresponding index. If necessary, the inductance can be extended by any harmonic [20].

The flux linkage of the permanent magnets is considered without higher order harmonics, as the focus is on the evaluation of the inductances. This results in

$$ {}^{(\mathrm{dq})}\vec{\Psi}_{\mathrm{PM}} = \begin{pmatrix} \Psi_{\mathrm{PM,d,0}} \\ 0 \end{pmatrix} . \tag{10} $$

In addition, the flux linkage of the permanent magnets is assumed to be independent of the current, as a measurement-based evaluation of this flux linkage is not part of this work. The time derivative of the flux linkage is calculated by the total differential [21], which yields

$$ \frac{\mathrm{d}}{\mathrm{d}t}\left({}^{(\mathrm{dq})}\vec{\Psi}\right) = \frac{\partial^{(\mathrm{dq})}\vec{\Psi}_{\mathrm{L}}}{\partial\gamma_{\mathrm{el}}}\frac{\mathrm{d}}{\mathrm{d}t}\gamma_{\mathrm{el}} + \frac{\partial^{(\mathrm{dq})}\vec{\Psi}_{\mathrm{L}}}{\partial {}^{(\mathrm{dq})}\vec{i}}\frac{\mathrm{d}}{\mathrm{d}t}{}^{(\mathrm{dq})}\vec{i} \ . \tag{11} $$

This results in an induced voltage due to the rotor position-dependent secant inductance with

$$ \begin{aligned} &\frac{\mathrm{d}}{\mathrm{d}t}\left(\mathbf{L}_{(\mathrm{dq})}\right){}^{(\mathrm{dq})}\vec{i} = -6\omega_{\mathrm{el}} \\ &\cdot\begin{pmatrix} L_{\mathrm{d},6}\sin\left(6\gamma_{\mathrm{el}}+\varphi_{\mathrm{d},6}\right) & L_{\mathrm{dq},6}\sin\left(6\gamma_{\mathrm{el}}+\varphi_{\mathrm{dq},6}\right) \\ L_{\mathrm{dq},6}\sin\left(6\gamma_{\mathrm{el}}+\varphi_{\mathrm{dq},6}\right) & L_{\mathrm{q},6}\sin\left(6\gamma_{\mathrm{el}}+\varphi_{\mathrm{q},6}\right) \end{pmatrix}{}^{(\mathrm{dq})}\vec{i} \end{aligned} \tag{12} $$

The differential inductance is likewise defined by

$$ \begin{aligned} \mathbf{L}'_{(\mathrm{dq})} &:= \frac{\partial^{(\mathrm{dq})}\vec{\Psi}_{\mathrm{L}}}{\partial {}^{(\mathrm{dq})}\vec{i}} = \begin{pmatrix} \frac{\partial\Psi_{\mathrm{L,d}}}{\partial i_{\mathrm{d}}} & \frac{\partial\Psi_{\mathrm{L,d}}}{\partial i_{\mathrm{q}}} \\ \frac{\partial\Psi_{\mathrm{L,q}}}{\partial i_{\mathrm{d}}} & \frac{\partial\Psi_{\mathrm{L,q}}}{\partial i_{\mathrm{q}}} \end{pmatrix} \\ &= \begin{pmatrix} L'_{\mathrm{d},0} & L'_{\mathrm{dq},0} \\ L'_{\mathrm{dq},0} & L'_{\mathrm{q},0} \end{pmatrix} \\ &+\begin{pmatrix} L'_{\mathrm{d},6}\cos\left(6\gamma_{\mathrm{el}}+\varphi'_{\mathrm{d},6}\right) & L'_{\mathrm{dq},6}\cos\left(6\gamma_{\mathrm{el}}+\varphi'_{\mathrm{dq},6}\right) \\ L'_{\mathrm{dq},6}\cos\left(6\gamma_{\mathrm{el}}+\varphi'_{\mathrm{dq},6}\right) & L'_{\mathrm{q},6}\cos\left(6\gamma_{\mathrm{el}}+\varphi'_{\mathrm{q},6}\right) \end{pmatrix} \end{aligned} \tag{13} $$

with a dependence on the rotor position, taking into account the sixth harmonic. For the differential inductance L' and its angles φ', the same notation for the indices is used as for the secant inductance. The sixth harmonic is chosen because it is the most significant harmonic of the device under test.

B. Model in the Estimated Reference Frame

For the model in the estimated reference frame, the rotor position error

$$ \gamma_{\mathrm{er}} = \gamma_{\mathrm{el}} - \hat{\gamma}_{\mathrm{el}} \tag{14} $$

with the estimated rotor position $\hat{\gamma}_{\mathrm{el}}$ is defined and the transformation matrix

$$ {}^{(\hat{\mathrm{d}}\hat{\mathrm{q}})}\mathbf{T}_{(\mathrm{dq})} = \begin{pmatrix} \cos(\gamma_{\mathrm{er}}) & -\sin(\gamma_{\mathrm{er}}) \\ \sin(\gamma_{\mathrm{er}}) & \cos(\gamma_{\mathrm{er}}) \end{pmatrix} \tag{15} $$

is used. The model of the PMSM in estimated coordinates is derived, using the model of the PMSM with the fundamental behavior

$$ {}^{(\mathrm{dq})}\vec{v} = R^{(\mathrm{dq})}\vec{i} + \mathbf{L}'_{(\mathrm{dq})}\frac{\mathrm{d}}{\mathrm{d}t}{}^{(\mathrm{dq})}\vec{i} + \mathbf{J}\omega_{\mathrm{el}}\mathbf{L}_{(\mathrm{dq})}{}^{(\mathrm{dq})}\vec{i} + \mathbf{J}\omega_{\mathrm{el}}{}^{(\mathrm{dq})}\vec{\Psi}_{\mathrm{PM}} \tag{16} $$

with

$$ {}^{(\mathrm{dq})}\vec{\Psi}_{\mathrm{PM}} = \begin{pmatrix} \Psi_{\mathrm{PM,d,0}} \\ 0 \end{pmatrix} \ , \ \mathbf{L}_{(\mathrm{dq})} = \begin{pmatrix} L_{\mathrm{d},0} & L_{\mathrm{dq},0} \\ L_{\mathrm{dq},0} & L_{\mathrm{q},0} \end{pmatrix} \tag{17} $$

and

$$ \mathbf{L}'_{(\mathrm{dq})} = \begin{pmatrix} L'_{\mathrm{d},0} & L'_{\mathrm{dq},0} \\ L'_{\mathrm{dq},0} & L'_{\mathrm{q},0} \end{pmatrix} \ . \tag{18} $$

The rotor position error γ_{er} is used and the equation is transformed into

$$ \begin{aligned} {}^{(\hat{\mathrm{d}}\hat{\mathrm{q}})}\vec{v} &= R^{(\hat{\mathrm{d}}\hat{\mathrm{q}})}\vec{i} + \mathbf{L}'_{(\hat{\mathrm{d}}\hat{\mathrm{q}})}\frac{\mathrm{d}}{\mathrm{d}t}{}^{(\hat{\mathrm{d}}\hat{\mathrm{q}})}\vec{i} + \mathbf{J}\omega_{\mathrm{el}}\mathbf{L}_{(\hat{\mathrm{d}}\hat{\mathrm{q}})}{}^{(\hat{\mathrm{d}}\hat{\mathrm{q}})}\vec{i} \\ &+ \mathbf{J}\omega_{\mathrm{er}}\mathbf{L}'_{(\hat{\mathrm{d}}\hat{\mathrm{q}})}{}^{(\hat{\mathrm{d}}\hat{\mathrm{q}})}\vec{i} + \mathbf{J}\omega_{\mathrm{el}}{}^{(\hat{\mathrm{d}}\hat{\mathrm{q}})}\vec{\Psi}_{\mathrm{PM}} \end{aligned} \tag{19} $$

with

$$ \begin{aligned} &{}^{(\hat{\mathrm{d}}\hat{\mathrm{q}})}\vec{v} = {}^{(\hat{\mathrm{d}}\hat{\mathrm{q}})}\mathbf{T}_{(\mathrm{dq})}{}^{(\mathrm{dq})}\vec{v} \ , \ {}^{(\hat{\mathrm{d}}\hat{\mathrm{q}})}\vec{i} = {}^{(\hat{\mathrm{d}}\hat{\mathrm{q}})}\mathbf{T}_{(\mathrm{dq})}{}^{(\mathrm{dq})}\vec{i} \\ &\omega_{\mathrm{er}} = \omega_{\mathrm{el}} - \hat{\omega}_{\mathrm{el}} \ , \ {}^{(\hat{\mathrm{d}}\hat{\mathrm{q}})}\vec{\Psi}_{\mathrm{PM}} = {}^{(\hat{\mathrm{d}}\hat{\mathrm{q}})}\mathbf{T}_{(\mathrm{dq})}{}^{(\mathrm{dq})}\vec{\Psi}_{\mathrm{PM}} \\ &\text{and} \ \ \mathbf{L}_{(\hat{\mathrm{d}}\hat{\mathrm{q}})} = {}^{(\hat{\mathrm{d}}\hat{\mathrm{q}})}\mathbf{T}_{(\mathrm{dq})}\mathbf{L}_{(\mathrm{dq})}{}^{(\mathrm{dq})}\mathbf{T}_{(\hat{\mathrm{d}}\hat{\mathrm{q}})} \ . \end{aligned} \tag{20} $$

The inductance in the estimated reference frame leads to

$$ \begin{aligned} \mathbf{L}_{(\hat{\mathrm{d}}\hat{\mathrm{q}})} &= \Sigma L\begin{pmatrix} 1 & 0 \\ 0 & 1 \end{pmatrix} + \Delta L\begin{pmatrix} \cos\left(2\gamma_{\mathrm{er}}\right) & \sin\left(2\gamma_{\mathrm{er}}\right) \\ \sin\left(2\gamma_{\mathrm{er}}\right) & -\cos\left(2\gamma_{\mathrm{er}}\right) \end{pmatrix} \\ &+ L_{\mathrm{dq},0}\begin{pmatrix} -\sin\left(2\gamma_{\mathrm{er}}\right) & \cos\left(2\gamma_{\mathrm{er}}\right) \\ \cos\left(2\gamma_{\mathrm{er}}\right) & \sin\left(2\gamma_{\mathrm{er}}\right) \end{pmatrix} \end{aligned} \tag{21} $$

with

$$ \Sigma L = \frac{L_{\mathrm{d},0}+L_{\mathrm{q},0}}{2} \quad \text{and} \quad \Delta L = \frac{L_{\mathrm{d},0}-L_{\mathrm{q},0}}{2} \ . \tag{22} $$

Based on the inductance in the estimated rotor-fixed reference frame, an approximation for small rotor position errors with

$$ \mathbf{L}_{(\hat{\mathrm{d}}\hat{\mathrm{q}})} = \begin{pmatrix} L_{\mathrm{d},0} & L_{\mathrm{dq},0} \\ L_{\mathrm{dq},0} & L_{\mathrm{q},0} \end{pmatrix} + 2\gamma_{\mathrm{er}}\begin{pmatrix} -L_{\mathrm{dq},0} & \Delta L \\ \Delta L & L_{\mathrm{dq},0} \end{pmatrix} \tag{23} $$

is applied [22]. The estimated differential inductance has the same shape, but is labeled with the symbol $'$.

C. Quasi-Direct (QD) Position Estimation

The QD calculation of [23], [24] with the nomenclature of [24] is used. The adaption law of the QD calculation is defined with

$$ \begin{aligned} &\hat{\gamma}_{\mathrm{er}}(k,i+1) = \hat{\gamma}_{\mathrm{er}}(k,i) \\ &-\frac{\eta}{2^{i-1}}\mathrm{sgn}\left[\left({}^{(\hat{\mathrm{d}}\hat{\mathrm{q}})}\mathfrak{J}_{\mathrm{FIE}}\left(\hat{\gamma}_{\mathrm{er}}(k,i)\right)^{T}{}^{(\hat{\mathrm{d}}\hat{\mathrm{q}})}\mathfrak{J}_{\mathrm{FIE}}\left(\hat{\gamma}_{\mathrm{er}}(k,i)\right)\right)^{-1}\right. \\ &\left.\cdot{}^{(\hat{\mathrm{d}}\hat{\mathrm{q}})}\mathfrak{J}_{\mathrm{FIE}}\left(\hat{\gamma}_{\mathrm{er}}(k,i)\right)^{T}\cdot{}^{(\hat{\mathrm{d}}\hat{\mathrm{q}})}\vec{r}_{\mathrm{FIE}}\left(\hat{\gamma}_{\mathrm{er}}(k,i)\right)\right] \ . \end{aligned} \tag{24} $$

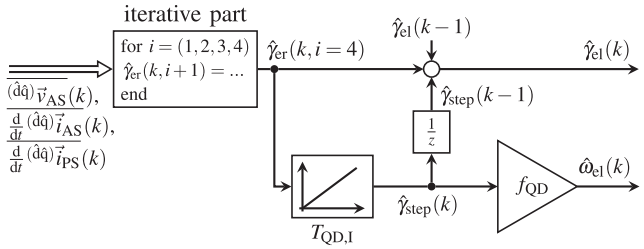

Fig. 1. Structure of the QD calculation [24].

The operator for a discrete sample is k. The Jacobian matrix is given by

$$ {}^{(\hat{\mathrm{dq}})}\mathfrak{J}_{\mathrm{FIE}} = \begin{pmatrix} \frac{\partial r_{\mathrm{d,FIE}}}{\partial \hat{\gamma}_{\mathrm{er}}} \\ \frac{\partial r_{\mathrm{q,FIE}}}{\partial \hat{\gamma}_{\mathrm{er}}} \end{pmatrix} = \frac{\partial}{\partial \hat{\gamma}_{\mathrm{er}}} {}^{(\hat{\mathrm{dq}})}\vec{r}_{\mathrm{FIE}} \quad . \tag{25} $$

The residual ${}^{(\hat{\mathrm{dq}})}\vec{r}_{\mathrm{FIE}}$ is derived in the next section. A basic structure for the quasi-direct (QD) calculation is shown in Fig. 1. Equation (24) is solved iteratively with the counter i and the calling rate of the QD calculation is f_{QD}. The speed is estimated via an integrator with the time constant $T_{\mathrm{QD,I}}$ [23]. The estimated speed is also used to feedforward the position change of each call of the estimator via the angle $\hat{\gamma}$step.

D. Residual With Consideration of a Mutual Inductance

The QD calculation optimizes a residual, which is derived from the stator voltage equation of the PMSM (19) [17]. An excitation with an SWI [6] at PWM frequency is required. Within [17], an integral over two consecutive passive switching states (PSs) and their following active switching states (ASs) are used to derive the residual. An example of a PWM period with injection of the SWI into the d-axis of the machine is shown in Fig. 2.

The upper plot in Fig. 2 shows the modulation indices (a_{a}^*, a_{b}^*, and a_{c}^*) of the three phases and the reference signal a_{ref} of the PWM generator. A fundamental voltage in the q-axis is present and the voltage of the d-axis alternates due to the SWI, which leads to the modulation indices shown and the voltages of the second plot of Fig. 2. In the third plot of Fig. 2, the terminal voltages of the PMSM are shown and the AS and PS of the converter are highlighted. The bottom plot shows the current of the PMSM with a colour-coded slope of the d-axis current in the AS and PS.

The differential equation of a PS yields

$$ \begin{aligned} \vec{0} = {} & R\overline{{}^{(\hat{\mathrm{dq}})}\vec{i}_{\mathrm{PS}}} + \omega_{\mathrm{el}}\mathbf{J}\mathbf{L}_{(\mathrm{dq})}\overline{{}^{(\hat{\mathrm{dq}})}\vec{i}_{\mathrm{PS}}} + \omega_{\mathrm{el}}\mathbf{J}^{(\hat{\mathrm{dq}})}\vec{\Psi}_{\mathrm{PM}} \\ & + \omega_{\mathrm{er}}\mathbf{J}\mathbf{L}'_{(\hat{\mathrm{dq}})}\overline{{}^{(\hat{\mathrm{dq}})}\vec{i}_{\mathrm{PS}}} + \mathbf{L}'_{(\mathrm{dq})}\overline{\frac{\mathrm{d}}{\mathrm{d}t}{}^{(\hat{\mathrm{dq}})}\vec{i}_{\mathrm{PS}}} \quad . \end{aligned} \tag{26} $$

For the two ASs of one PWM half-period, the differential equation is

$$ \begin{aligned} \overline{{}^{(\hat{\mathrm{dq}})}v_{\mathrm{AS}}} = {} & R\overline{{}^{(\hat{\mathrm{dq}})}\vec{i}_{\mathrm{AS}}} + \omega_{\mathrm{el}}\mathbf{J}\mathbf{L}_{(\mathrm{dq})}\overline{{}^{(\hat{\mathrm{dq}})}\vec{i}_{\mathrm{AS}}} + \omega_{\mathrm{el}}\mathbf{J}^{(\hat{\mathrm{dq}})}\vec{\Psi}_{\mathrm{PM}} \\ & + \omega_{\mathrm{er}}\mathbf{J}\mathbf{L}'_{(\hat{\mathrm{dq}})}\overline{{}^{(\hat{\mathrm{dq}})}\vec{i}_{\mathrm{AS}}} + \mathbf{L}'_{(\mathrm{dq})}\overline{\frac{\mathrm{d}}{\mathrm{d}t}{}^{(\hat{\mathrm{dq}})}\vec{i}_{\mathrm{AS}}} \quad . \end{aligned} \tag{27} $$

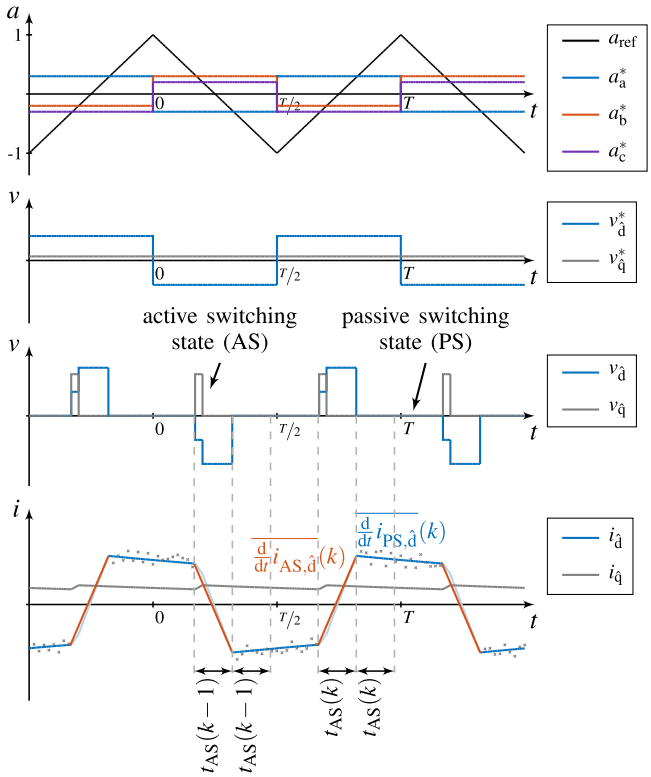

Fig. 2. Voltage and current of the PMSM during a PWM period with SWI.

In both equations, the variables used are assumed to be their mean values over the switching state (marked with $^-$) and denoted by the indices PS and AS, respectively.

The integrals over the ASs and PS of one PWM half-period are subtracted from one another to eliminate the fundamental components. The time interval for both integrals is the length of the ASs t_{AS}. In addition, the intermediate results from two consecutive PWM half-periods are subtracted from each other to compensate for measurement errors. Details of these steps can be found in [17]. To distinguish between the values of the two PWM half-periods, the discrete variable k is used. As a result, the equation

$$ \begin{aligned} 0 = {} & {}^{(\mathrm{dq})}\vec{v}^*(k-1) - {}^{(\mathrm{dq})}\vec{v}^*(k) \\ & - \mathbf{L}'_{(\mathrm{dq})}\frac{2t_{\mathrm{AS}}(k-1)}{T}\left[\overline{\frac{\mathrm{d}}{\mathrm{d}t}{}^{(\mathrm{dq})}\vec{i}_{\mathrm{AS}}}(k-1)\right. \\ & \left. - \overline{\frac{\mathrm{d}}{\mathrm{d}t}{}^{(\mathrm{dq})}\vec{i}_{\mathrm{PS}}}(k-1)\right] \\ & + \mathbf{L}'_{(\mathrm{dq})}\frac{2t_{\mathrm{AS}}(k)}{T}\left[\overline{\frac{\mathrm{d}}{\mathrm{d}t}{}^{(\mathrm{dq})}\vec{i}_{\mathrm{AS}}}(k) - \overline{\frac{\mathrm{d}}{\mathrm{d}t}{}^{(\mathrm{dq})}\vec{i}_{\mathrm{PS}}}(k)\right] \end{aligned} \tag{28} $$

is derived. This equation is simplified by the substitution of the current increments

$$ \begin{aligned} & \frac{\Delta}{\Delta t}{}^{(\mathrm{dq})}\vec{i}(k-1) \\ & = \frac{2t_{\mathrm{AS}}(k-1)}{T}\left[\overline{\frac{\mathrm{d}}{\mathrm{d}t}{}^{(\mathrm{dq})}\vec{i}_{\mathrm{AS}}}(k-1) + \overline{\frac{\mathrm{d}}{\mathrm{d}t}{}^{(\mathrm{dq})}\vec{i}_{\mathrm{PS}}}(k-1)\right] \end{aligned} $$

$$\frac{\Delta}{\Delta t}{}^{(\mathrm{dq})}\vec{i}(k) = \frac{2t_{\mathrm{AS}}(k)}{T}\left[\overline{\frac{\mathrm{d}}{\mathrm{d}t}{}^{(\mathrm{dq})}\vec{i}_{\mathrm{AS}}}(k) + \overline{\frac{\mathrm{d}}{\mathrm{d}t}{}^{(\mathrm{dq})}\vec{i}_{\mathrm{PS}}}(k)\right]. \tag{29}$$

This leads to the equation

$$0 = {}^{(\mathrm{dq})}\vec{v}^{*}(k) - {}^{(\mathrm{dq})}\vec{v}^{*}(k-1) + \mathbf{L}'_{(\mathrm{dq})}\left[\frac{\Delta}{\Delta t}{}^{(\mathrm{dq})}\vec{i}(k-1) - \frac{\Delta}{\Delta t}{}^{(\mathrm{dq})}\vec{i}(k)\right] \tag{30}$$

which is used in the estimated reference frame as the residual

$${}^{(\hat{\mathrm{dq}})}\vec{r}_{\mathrm{FIE}} = {}^{(\hat{\mathrm{dq}})}\vec{v}^{*}(k) - {}^{(\hat{\mathrm{dq}})}\vec{v}^{*}(k-1) + \mathbf{L}'_{(\hat{\mathrm{dq}})}\left[\frac{\Delta}{\Delta t}{}^{(\hat{\mathrm{dq}})}\vec{i}(k-1) - \frac{\Delta}{\Delta t}{}^{(\hat{\mathrm{dq}})}\vec{i}(k)\right] \tag{31}$$

of the flux increment estimator (FIE) with the differential inductance matrix being dependent on the rotor position error [cf. (23)]. In order to use the residual in the QD calculation, its Jacobian

$$\begin{aligned}{}^{(\hat{\mathrm{dq}})}\mathfrak{J}_{\mathrm{FIE}} &= \begin{pmatrix}\frac{\partial \tilde{r}_{\mathrm{d,FIE}}}{\partial\hat{\gamma}_{\mathrm{er}}}\\ \frac{\partial r_{\mathrm{q,FIE}}}{\partial\hat{\gamma}_{\mathrm{er}}}\end{pmatrix} = \frac{\partial}{\partial\hat{\gamma}_{\mathrm{er}}}{}^{(\hat{\mathrm{dq}})}\vec{r}_{\mathrm{FIE}}\\ &= 2\begin{pmatrix}-L'_{\mathrm{dq},0} & \Delta L'\\ \Delta L' & L'_{\mathrm{dq},0}\end{pmatrix}\left[\frac{\Delta}{\Delta t}{}^{(\hat{\mathrm{dq}})}\vec{i}(k-1) - \frac{\Delta}{\Delta t}{}^{(\hat{\mathrm{dq}})}\vec{i}(k)\right]\end{aligned} \tag{32}$$

is calculated. Note that the mutual inductance of the PMSM is inherently used.

E. Residual Without Consideration of a Mutual Inductance

In order to obtain a comparison of a rotor position estimation method with and without the consideration of mutual inductances, the residual is derived without the use of the mutual inductance. Not using the mutual inductance within the derivation is a common practice in SSC. This is only for the purpose of comparing the results on the same test bench with the same rotor position estimator.

The residual of the FIE is

$${}^{(\hat{\mathrm{dq}})}\tilde{\vec{r}}_{\mathrm{FIE}} = {}^{(\hat{\mathrm{dq}})}\vec{v}^{*}(k) - {}^{(\hat{\mathrm{dq}})}\vec{v}^{*}(k-1) + \tilde{\mathbf{L}}'_{(\hat{\mathrm{dq}})}\left[\frac{\Delta}{\Delta t}{}^{(\hat{\mathrm{dq}})}\vec{i}(k-1) - \frac{\Delta}{\Delta t}{}^{(\hat{\mathrm{dq}})}\vec{i}(k)\right]. \tag{33}$$

Modifying the residual to give the variant, which does not use the mutual inductance, the differential inductance matrix becomes

$$\tilde{\mathbf{L}}'_{(\hat{\mathrm{dq}})} = \Sigma L'\begin{pmatrix}1 & 0\\ 0 & 1\end{pmatrix} + 2\gamma_{\mathrm{er}}\begin{pmatrix}0 & \Delta L'\\ \Delta L' & 0\end{pmatrix} \tag{34}$$

with ($L_{\mathrm{dq}} = 0$). This leads to the Jacobian

$$\tilde{\mathfrak{J}}_{\mathrm{FIE}} = \begin{pmatrix}\frac{\partial \tilde{r}_{\mathrm{d,FIE}}}{\partial\hat{\gamma}_{\mathrm{er}}}\\ \frac{\partial \tilde{r}_{\mathrm{q,FIE}}}{\partial\hat{\gamma}_{\mathrm{er}}}\end{pmatrix} = \frac{\partial}{\partial\hat{\gamma}_{\mathrm{er}}}{}^{(\hat{\mathrm{dq}})}\tilde{\vec{r}}_{\mathrm{FIE}} = 2\begin{pmatrix}0 & \Delta L'\\ \Delta L' & 0\end{pmatrix}\left[\frac{\Delta}{\Delta t}{}^{(\hat{\mathrm{dq}})}\vec{i}(k-1) - \frac{\Delta}{\Delta t}{}^{(\hat{\mathrm{dq}})}\vec{i}(k)\right]. \tag{35}$$

which only has entities on the secondary diagonal.

TABLE I
PMSM RATED VALUES AND MACHINE DATA

Rated current (RMS)	I_{r}	6.7 A
Rated torque	M_{r}	0.5 N·m
Rated rotational speed	n_{r}	5850 min^{-1}
Phase resistance	R	0.39 Ω
Flux linkage	Ψ_{PM}	8.05 mVs
Number of pole pairs	p	4

TABLE II
CONTROL AND ESTIMATOR PARAMETERS USED

P-gain current control	$K_{\mathrm{FDE\text{-}QD,i,P}}$	1.5 $\mathrm{V/A}$
Time const. current control	$T_{\mathrm{FDE\text{-}QD,i,N}}$	0.5 ms
Iterations	l_{QD}	4
Initial step width	$\eta_{\mathrm{FDE\text{-}QD}}$	$5.4\cdot10^{-3}$ rad
Integrator time const.	$T_{\mathrm{QD,I}}$	3.3 ms
SWI amplitude	v_{HF}	5 V
P-gain speed control	$K_{\mathrm{FDE\text{-}QD},\omega,\mathrm{P}}$	0.061 A · min
Time const. speed control	$T_{\mathrm{FDE\text{-}QD},\omega,\mathrm{N}}$	15.9 ms
P-gain position control	$K_{\gamma,\mathrm{P}}$	70 $\frac{1}{\mathrm{rad\cdot min}}$

F. Experimental Test Setup

For the experimental investigation, a rapid prototyping system is used, which consists of a Xilinx Zynq 7000 System-on-a-Chip (SoC). The structure of the control is shown in Fig. 3. As an input, the setpoint of the rotor position γ^{*}_{el}, controlled by a P-controller, is used. The setpoint of the rotor speed ω^{*}_{el} is fed through a low-pass filter (LPF) to the PI-controller for the rotor speed. A maximum torque per current control strategy is used to define the setpoint current ${}^{(\hat{\mathrm{dq}})}\vec{i}^{*}$ for the FOC, using the setpoint of torque M^{*} as an input. The HF voltage ${}^{(\hat{\mathrm{dq}})}\vec{v}^{*}$ is added to the setpoint of the FOC, which yields the output voltage of the converter ${}^{(\hat{\mathrm{dq}})}\vec{v}^{*}$. This voltage is transformed into the stator-fixed reference frame and used to generate the gate signals of the converter $\vec{g}_{1..6}$ via a PWM generator. The converter has a dc-link voltage of 48V and a switching frequency of $f_{\mathrm{PWM}} = 10\,\mathrm{kHz}$.

The analogue-to-digital converter for shunt-based current measurement are driven by the programmable logic (PL) with a sampling frequency of 1 Mb/s. The current measurement is limited by an analogue LPF to a bandwidth of 600 kHz and a digital grey-box model filter is used to reduce the influence of parasitic effects of the machine according to [25], [26]. Due to the high sampling rate, the slopes of the currents within a PWM period can be determined by a least mean squares algorithm in the PL. In addition, a field programmable gate array-based high-dynamic dead-time compensation [27] is used. The rated values of the machine under test are given in Table I.

The device under test is connected to a load machine via a torque measuring shaft as shown in Fig. 4. The combined inertia of the system is $0.2578\cdot10^{-3}\,\mathrm{kg\cdot m^2}$.

For the estimator, position control, speed control, and FOC, the parameters of Table II are used. The current control of the

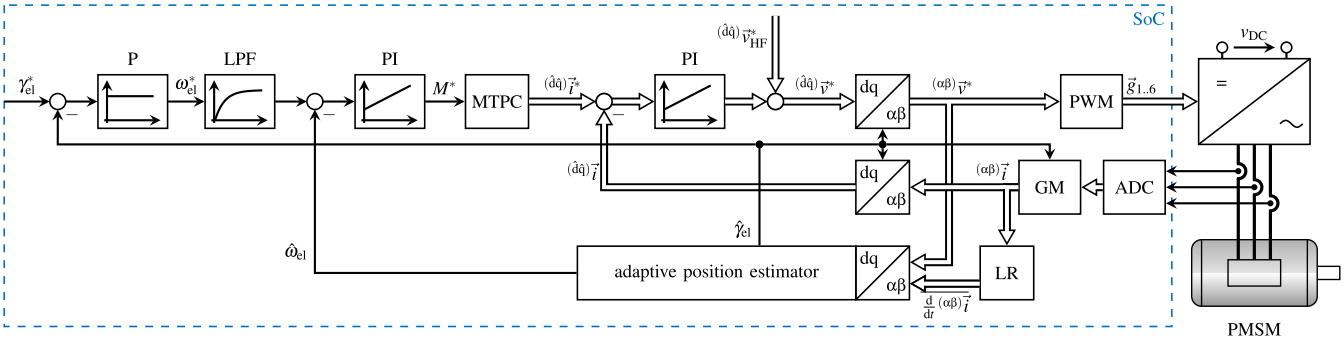

Fig. 3. Block diagram of the FOC as SSC (based on [23]).

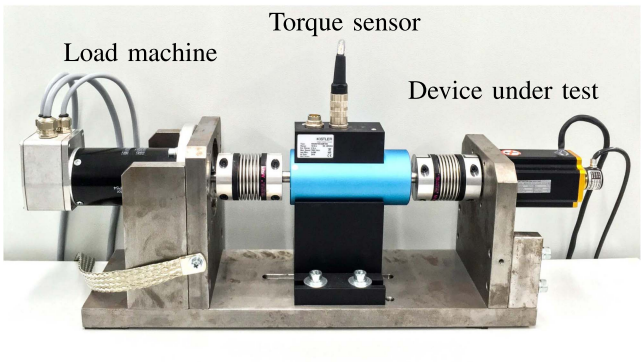

Fig. 4. Test bench.

FOC is tuned using the method of an optimal amount. The speed control and the parameters of the FIE-QD are set according to the analytical solution of [24] with a time constant from the QD calculation of $T_{\mathrm{QD,I}} = 3.3\,\mathrm{ms}$. The position control is tuned empirically.

III. Determination of the Inductance Matrix

The proposed method for SSC is dependent on the values of the inductance matrix. Thus, a determination method or a calculation of the machine parameters is mandatory. Here, a determination process for the inductances is proposed, which uses the residual of the FIE-QD and the mounted encoder.

The following determination process is performed for every measured rotor position and every operating point of the machine. To simplify the equations, the determination process is shown for one rotor position and one operating point.

Using the measured rotor position, the residual is assumed to be zero

$$ {}^{(\mathrm{dq})}\vec{r}_{\mathrm{FIE}} = {}^{(\mathrm{dq})}\vec{v}_{\mathrm{FIE}} - \mathbf{L}'_{(\hat{\mathrm{d}}\hat{\mathrm{q}})} \frac{\Delta}{\Delta t} {}^{(\mathrm{dq})}\vec{i}_{\mathrm{FIE}} = \vec{0}\ . \tag{36} $$

Here, the simplification

$$ {}^{(\mathrm{dq})}\vec{v}_{\mathrm{FIE}} = {}^{(\mathrm{dq})}\vec{v}^{*}(k) - {}^{(\mathrm{dq})}\vec{v}^{*}(k-1) \tag{37} $$

and

$$ \frac{\Delta}{\Delta t} {}^{(\mathrm{dq})}\vec{i}_{\mathrm{FIE}} = \frac{\Delta}{\Delta t} {}^{(\mathrm{dq})}\vec{i}(k) - \frac{\Delta}{\Delta t} {}^{(\mathrm{dq})}\vec{i}(k-1) \tag{38} $$

are used. To determine the inductances, three linearly independent voltages

$$ {}^{(\mathrm{dq})}\vec{v}_{\mathrm{FIE,M1}} = {}^{(\mathrm{dq})}\vec{v}_{\mathrm{FOC}} + \begin{pmatrix} \pm v_{\mathrm{HF}} \\ 0 \end{pmatrix} \tag{39} $$

$$ {}^{(\mathrm{dq})}\vec{v}_{\mathrm{FIE,M2}} = {}^{(\mathrm{dq})}\vec{v}_{\mathrm{FOC}} + \begin{pmatrix} 0 \\ \pm v_{\mathrm{HF}} \end{pmatrix} \tag{40} $$

and

$$ {}^{(\mathrm{dq})}\vec{v}_{\mathrm{FIE,M3}} = {}^{(\mathrm{dq})}\vec{v}_{\mathrm{FOC}} \pm v_{\mathrm{HF}} \begin{pmatrix} 1 \\ 1 \end{pmatrix} \tag{41} $$

are injected for each rotor position. Combining the three independent voltages and the residual (36), the overdetermined system of equations for one rotor position and one operating point

$$ \begin{aligned} 0 = &\begin{bmatrix} {}^{(\mathrm{dq})}\vec{v}_{\mathrm{FIE,M1}} & {}^{(\mathrm{dq})}\vec{v}_{\mathrm{FIE,M2}} & {}^{(\mathrm{dq})}\vec{v}_{\mathrm{FIE,M3}} \end{bmatrix} \\ &- \mathbf{L}'_{(\mathrm{dq})} \begin{bmatrix} \frac{\Delta}{\Delta t} {}^{(\mathrm{dq})}\vec{i}_{\mathrm{FIE,M1}} & \frac{\Delta}{\Delta t} {}^{(\mathrm{dq})}\vec{i}_{\mathrm{FIE,M2}} & \frac{\Delta}{\Delta t} {}^{(\mathrm{dq})}\vec{i}_{\mathrm{FIE,M3}} \end{bmatrix} \end{aligned} \tag{42} $$

is defined. This system of equations is solved via an offline nonlinear numerical optimization. As a further constraint, the mutual inductances on the secondary diagonal are assumed to be identical, that is, $L'_{\mathrm{dq}} = L'_{\mathrm{qd}}$. The optimization problem is set up by defining the function

$$ \begin{aligned} \mathbf{A}(\mathbf{L}'_{(\mathrm{dq})}) = &\begin{bmatrix} {}^{(\mathrm{dq})}\vec{v}_{\mathrm{FIE,M1}} & {}^{(\mathrm{dq})}\vec{v}_{\mathrm{FIE,M2}} & {}^{(\mathrm{dq})}\vec{v}_{\mathrm{FIE,M3}} \end{bmatrix} \\ &- \mathbf{L}'_{(\mathrm{dq})} \begin{bmatrix} \frac{\Delta}{\Delta t} {}^{(\mathrm{dq})}\vec{i}_{\mathrm{FIE,M1}} & \frac{\Delta}{\Delta t} {}^{(\mathrm{dq})}\vec{i}_{\mathrm{FIE,M2}} & \frac{\Delta}{\Delta t} {}^{(\mathrm{dq})}\vec{i}_{\mathrm{FIE,M3}} \end{bmatrix} \end{aligned} \tag{43} $$

with

$$ \mathbf{A}(\mathbf{L}'_{(\mathrm{dq})}) = \begin{bmatrix} a_{11}(\mathbf{L}'_{(\mathrm{dq})}) & a_{12}(\mathbf{L}'_{(\mathrm{dq})}) & a_{13}(\mathbf{L}'_{(\mathrm{dq})}) \\ a_{21}(\mathbf{L}'_{(\mathrm{dq})}) & a_{22}(\mathbf{L}'_{(\mathrm{dq})}) & a_{23}(\mathbf{L}'_{(\mathrm{dq})}) \end{bmatrix} . \tag{44} $$

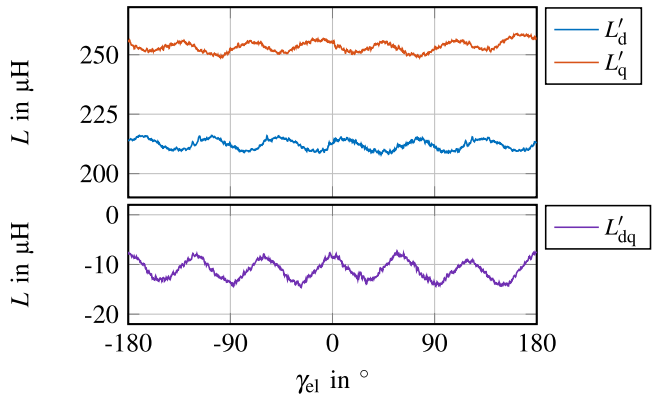

Fig. 5. Determined inductances at $i_q = 10\,\mathrm{A}$, $i_d = 0\,\mathrm{A}$ and over one electrical revolution.

In addition, the cost function

$$C(\mathbf{L}'_{(dq)}) = \sqrt{\sum_{i=1}^{2}\sum_{j=1}^{3}|a_{ij}(\mathbf{L}'_{(dq)})|^2} \tag{45}$$

is used. By using a nonlinear optimization, the minimum of the cost function

$$\mathbf{L}'_{(dq)} = \arg\min_{\mathbf{L}'_{(dq)}} C(\mathbf{L}'_{(dq)}) \tag{46}$$

is searched for by varying the values of the inductances. This yields the example result according to Fig. 5 for a q-current of $i_q = 10\,\mathrm{A}$, a d-current of $i_d = 0\,\mathrm{A}$, and over one electrical revolution.

These results are generated for each operating point over one electrical revolution. Through the use of a fast Fourier transform (FFT), the direct component (shown in Fig. 6) and the sixth harmonic (shown in Fig. 7) of the inductances are determined.

Each result in Fig. 6 shows valid behavior for the direct component of the inductances. The self-inductances decrease as the machine saturates ($i_d > 0\,\mathrm{A}$ or $|i_q| > 0\,\mathrm{A}$) and increase as the machine is desaturated ($i_d < 0\,\mathrm{A}$). For the mutual inductance, the values increase with increasing q-current, while the sign of the mutual inductance alters with reference to the q-current. The quality of the results for the direct component of the inductances shows a high signal-to-noise ratio compared to previous work (cf. [23]), due to the value being determined over a whole electrical revolution, which consists of 2000 individual rotor positions.

All three magnitudes of the sixth harmonics of the inductances of Fig. 7 show qualitatively similar curves, whereby the magnitude of the sixth harmonic increases with increasing saturation of the stator yoke. When looking at the phase of the sixth harmonic, a phase shift of approximately π between the d-axis and q-axis becomes apparent. The mutual inductance has a phase shift of $\pi/2$ relative to the d-axis. Overall, the inductance curve can, thus, be approximated as

$$\mathbf{L}'_{(dq)} = \begin{pmatrix} L'_{d,0} & L'_{dq,0} \\ L'_{dq,0} & L'_{q,0} \end{pmatrix}$$

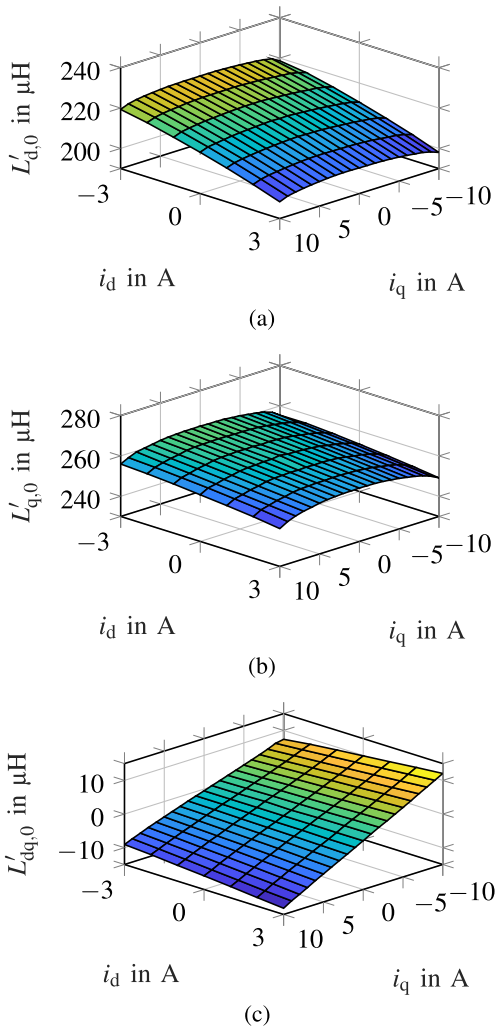

Fig. 6. Measured direct component of the differential inductances of the PMSM. (a) $L'_{d,0}$. (b) $L'_{q,0}$. (c) $L'_{dq,0}$.

$$+ \mathbf{R}(\alpha_6 + 6\gamma_{el}) \begin{pmatrix} \Delta L'_6 & 0 \\ 0 & -\Delta L'_6 \end{pmatrix} . \tag{47}$$

For this purpose

$$\mathbf{R}\left(\alpha_6 + 6\gamma_{el}\right) = \begin{pmatrix} \cos\left(\alpha_6 + 6\gamma_{el}\right) & \sin\left(\alpha_6 + 6\gamma_{el}\right) \\ -\sin\left(\alpha_6 + 6\gamma_{el}\right) & \cos\left(\alpha_6 + 6\gamma_{el}\right) \end{pmatrix} \tag{48}$$

is used. The value of the inductance is $\Delta L'_6$ and the phase is α_6. A modified inductance has been used on the test bench. This is described by

$$\mathbf{L}'_{(dq)} = \begin{pmatrix} L'_{d,0} & L'_{dq,0} \\ L'_{dq,0} & L'_{q,0} \end{pmatrix} + \mathbf{R}(\alpha^*_6 + 6\gamma_{el}) \begin{pmatrix} -\Delta L'_6 & 0 \\ 0 & \Delta L'_6 \end{pmatrix} \tag{49}$$

with

$$\alpha^*_6 = \alpha_6 - \pi \ . \tag{50}$$

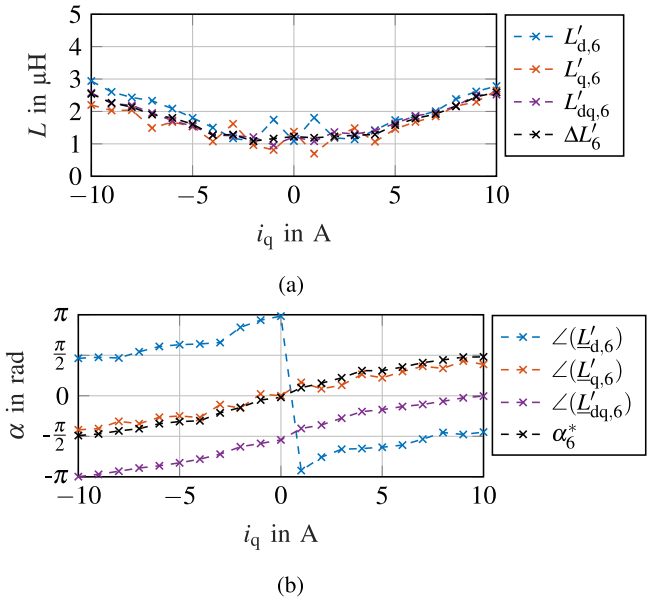

Fig. 7. Determined magnitude and phase of the sixth harmonic of the inductances against the q-current at a d-current of $i_d = 0$ A. (a) Magnitude. (b) Phase.

The phase α_6^* was chosen to avoid a phase jump in the result. This allows the result to be stored in a look-up table without causing a problem when interpolating. To determine the inductance and phase, the complex inductance

$$\begin{aligned}\Delta\underline{L}'_6 &= \frac{1}{3}\left(-\underline{L}'_{d,6} + \underline{L}'_{q,6} + \underline{L}'_{dq,6}\cdot e^{j\frac{\pi}{2}}\right)\\ &= \frac{L'_{d,6}\left(\cos(\angle(\underline{L}'_{d,6})+\pi) + j\sin(\angle(\underline{L}'_{d,6})+\pi)\right)}{3}\\ &\quad + \frac{L'_{q,6}\left(\cos(\angle(\underline{L}'_{q,6})) + j\sin(\angle(\underline{L}'_{q,6}))\right)}{3}\\ &\quad + \frac{L'_{dq,6}\left(\cos(\angle(\underline{L}'_{dq,6})+\pi/2) + j\sin(\angle(\underline{L}'_{dq,6})+\pi/2)\right)}{3}\end{aligned} \tag{51}$$

is used and the magnitude and phase are calculated as

$$\Delta L'_6 = |\Delta\underline{L}'_6| \quad \text{and} \quad \alpha_6^* = \angle(\Delta\underline{L}'_6) \quad . \tag{52}$$

The results for the sixth harmonic magnitude $\Delta L'_6$ and phase α_6^* are shown in Fig. 7(a) and (b).

IV. Effect of the Mutual Inductance

In this section, the effect of a noncompensated mutual inductance and the use of the mutual inductance within the residual of the estimator are investigated.

A. Simulation Results

In simulations, a synthetic parameterization of the machine is possible. This is used to compare the residuals with and without the use of the mutual inductance. For this purpose, the mutual inductance is set to rise proportional to the q-current to achieve the results of Fig. 8. On the left, the mutual inductance is not used within the residual, while on the right, the mutual inductance is used.

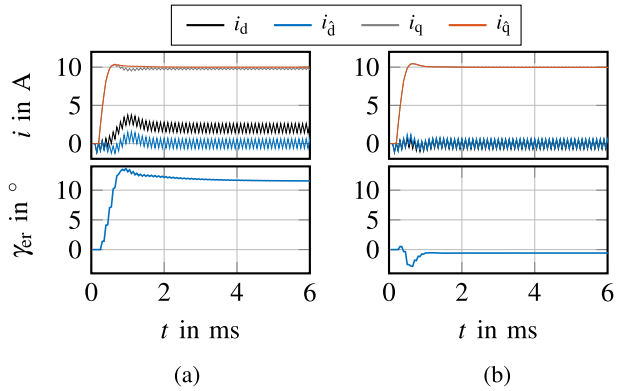

Fig. 8. Comparison of the rotor position error with and without consideration of L'_{dq} for $L'_d(i_q = 10\,\text{A}) = 205\,\mu\text{H}$, $L'_q(i_q = 10\,\text{A}) = 250\,\mu\text{H}$ and $L'_{dq}(i_q = 10\,\text{A}) = 9.5\,\mu\text{H}$. (a) Without compensation of L'_{dq}. (b) With compensation of L'_{dq}.

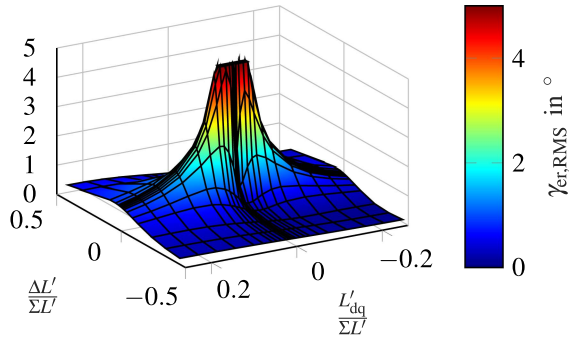

Fig. 9. RMS value of the rotor position error against different values of the difference of the self-inductances $\Delta L'$ and the mutual inductance L'_{dq}.

Using an estimator which does not account for a mutual inductance [shown in Fig. 8(a)] and which uses an alternating signal for estimation, the stationary estimation error is given by

$$\gamma_{er} = -\frac{1}{2}\text{atan}\left(\frac{L'_{dq,0}}{\Delta L'}\right) \tag{53}$$

which is widely known in the literature [11], [18], [28]. In the result of Fig. 8(b), no stationary estimation error arises, due to the use of the mutual inductance within the residual of the estimator. Only small estimation errors occur in the transient states.

An additional opportunity lies in the use of the mutual inductance as a source of information for anisotropy-based SSC. When using the mutual inductance within the residual, the position can be estimated even at operating points with equal self-inductances of the d-axis and q-axis ($L'_d = L'_q$) and a sufficient mutual inductance ($L'_{dq} \neq 0$). This is shown in Fig. 9. The difference between the self-inductances $\Delta L'$ and the mutual inductance L'_{dq} are varied in simulations and the root mean square (RMS) of the rotor position estimation error over one electrical period is plotted for each combination of $\Delta L'$ and L'_{dq}.

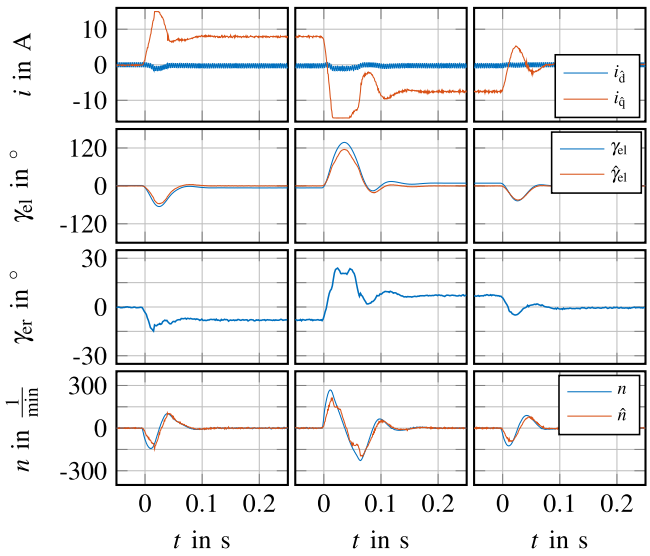

Fig. 10. Closed-loop SSC in position control without compensation of the mutual inductance. Rated torque is applied (left), reversed (centre), and reduced to zero (right).

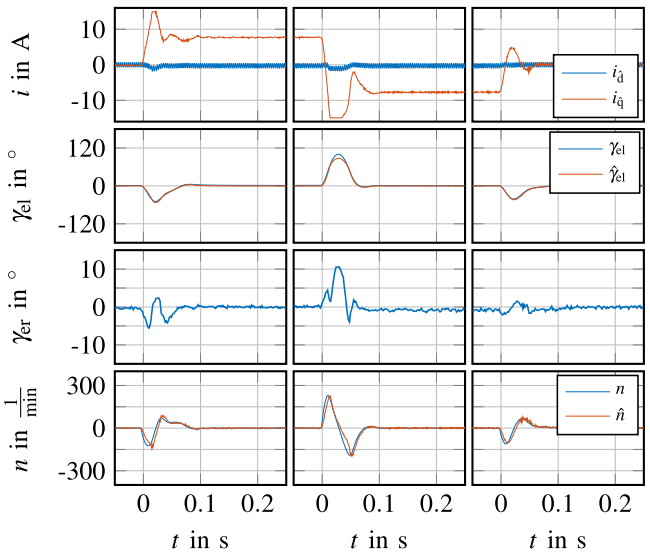

Fig. 11. Closed-loop SSC in position control with compensation of the mutual inductance. Rated torque is applied (left), reversed (centre), and reduced to zero (right).

The results show that the estimation of the rotor position only fails for the points where both the difference between the self-inductances $\Delta L'$ and the mutual inductance L'_{dq} are small. The other points can be estimated with a low estimation error. This result is only shown for the residual using the mutual inductance, because the variant which does not use the mutual inductance becomes unstable for the points with a small difference between the self-inductances $\Delta L'$. In addition, the stationary estimation error for this variant is known [11], [18], [28].

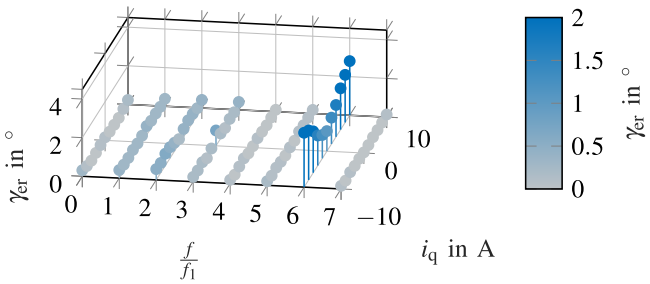

Fig. 12. Spectrum of the steady-state rotor position estimation error using the compensation of the mutual inductance at $n = 20\,{}^{1}/_{\mathrm{min}}$ and different q-currents.

B. Experimental Validation

To evaluate the compensation of the mutual inductance, the device under test is position controlled and different loads are applied via the load machine. The load torque steps from zero load to rated torque, and then the rated torque is reversed and finally set back to zero. The results without compensation of the mutual inductance are shown in Fig. 10.

In the first row, the currents are shown. The second row shows the measured and estimated rotor positions, followed by the rotor position error. In the last row, the measured and estimated speeds are shown. In the results, the rotor position estimation remains stable and the estimated position $\hat{\gamma}_{\mathrm{el}}$ is controlled to zero degrees in stationary states. While the device under test is stationary, the expected rotor position error caused by the mutual inductance is present. In transient states, a harmonic error and a speed-dependent error are superimposed on the error of the stationary state.

The next results are obtained with compensation of the mutual inductance and are shown in Fig. 11.

Again, the rotor position remains stable, but the estimation error decreases to zero in the steady state. Both the harmonic error and the speed-dependent error only arise in transient states, validating the compensation of the mutual inductance experimentally. It should be noted that the estimation error during transients is reduced as well.

To quantify the remaining harmonic error, an FFT of the rotor position error in the steady state for different q-currents over an electrical revolution at $n = 20\,{}^{1}/_{\mathrm{min}}$ is shown in Fig. 12.

As the results show, there is only a sixth harmonic error present. The other harmonics and the direct component are below $0.5°$ in magnitude. This motivates the investigation of the sixth harmonic, which is carried out in the following section.

C. Parameter Sensitivity

In the following, the parameter sensitivity of the estimator is investigated. For this purpose, the values of the difference in self-inductances and the mutual inductance used in the estimator are varied according to

$$L'_{\mathrm{d,est}} = L'_{\mathrm{d},0} + \Delta L'_{\mathrm{off}} \quad , \quad L'_{\mathrm{q,est}} = L'_{\mathrm{q},0} - \Delta L'_{\mathrm{off}} \tag{54}$$

$$\Delta L'_{\mathrm{est}} = \Delta L' + \Delta L'_{\mathrm{off}} \quad \text{and} \quad L'_{\mathrm{dq,est}} = L'_{\mathrm{dq},0} + L'_{\mathrm{dq,off}}. \tag{55}$$

This parameter variation is done in two different operating points with different differences in self-inductances and mutual

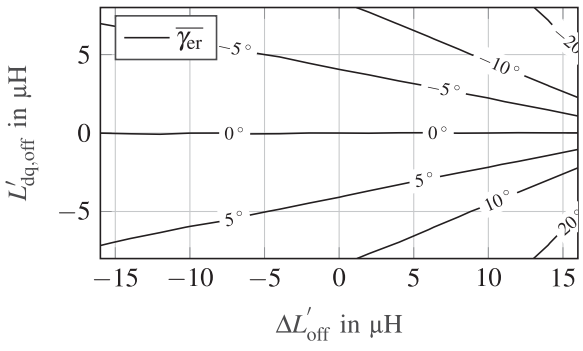

(a)

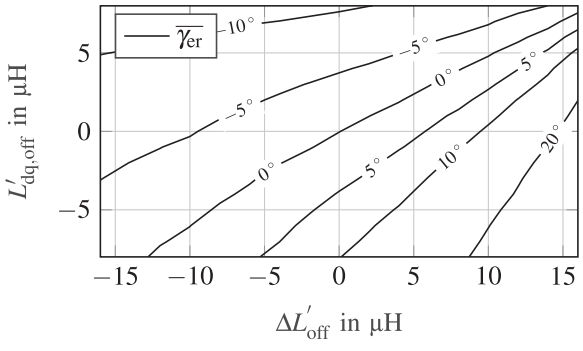

(b)

Fig. 13. Mean value of the rotor position error $\overline{\gamma_{er}}$ against different offset values of the difference of the self-inductances $\Delta L'_{off}$ and the mutual inductance $L'_{dq,off}$ at two different operating points. (a) $i_{\hat{q}} = 0$ A, $\Delta L' = -22.7$ μH and $L'_{dq,0} = 0$ μH. (b) $i_{\hat{q}} = 10$ A, $\Delta L' = -21.5$ μH and $L'_{dq,0} = -10.9$ μH.

inductances. The result for the mean value of the estimation error over an electrical revolution at $n = 20\,{}^1/_{\text{min}}$ is shown in Fig. 13.

In Fig. 13(a), an operating point with no mutual inductance is shown. Here, the mean value of the estimation error remains zero, when the offset value of the mutual inductance $L'_{dq,off}$ is zero. For values of the offset of the mutual inductance unequal to zero, the mean value of the estimation error is approximated by

$$\gamma_{er} = \frac{1}{2}\text{atan}\left(\frac{L'_{dq,est}}{\Delta L'_{est}}\right) \quad \text{for} \quad L'_{dq,0} = 0\ \mu\text{H} \quad . \tag{56}$$

Thus, the mean value of the position error has the same magnitude as the error for an uncompensated mutual inductance of (53), but with an alternating sign.

The result of Fig. 13(b) shows the behavior with a mutual inductance. In this case, the mean value of the estimation error remains zero for a diagonal line on the plot. In both cases, the mean value of the estimation error remains zero if the ratio of the mutual inductance and the difference in self-inductances remains unchanged. Specifically, the values used by the estimator must meet the requirements

$$\Delta L'_{est} = c \cdot \Delta L' \quad \text{and} \quad L'_{dq,est} = c \cdot L'_{dq,0} \tag{57}$$

with c being a positive real number unequal to zero

$$c \in \mathbb{R}^+ \quad . \tag{58}$$

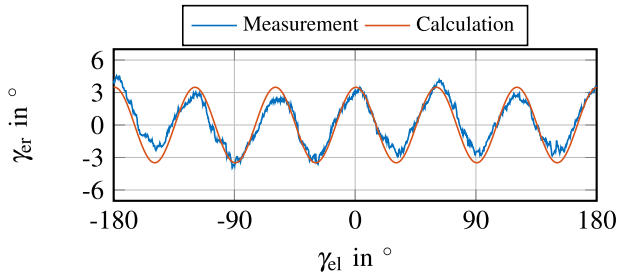

Fig. 14. Rotor position error over one electrical revolution at $n = 20\,{}^1/_{\text{min}}$, $i_{\hat{q}} = 10$ A, and $i_{\hat{d}} = 0$ A.

This behavior is a positive feature of the estimator, because the amplitudes of the inductances are not of importance. Only the relative values of the inductances must be measured, which reduces the influence of systematic errors within the determination of the inductances.

V. Effect of the Multiple Saliency

First, an analytical equation to calculate the resulting estimation error due to a higher order saliancy is derived. Then, the error due to the higher order saliancy is compensated.

A. Analytical Calculation of the Rotor Position Error

To analytically describe the estimation error due to a multiple saliency, the point of convergence is sought. At the point of convergence, the inductance matrix without the sixth harmonic is equal to the inductance matrix with the sixth harmonic. The degree of freedom is a rotor position error between the two inductance matrices. The equation results in

$$\begin{aligned} &{}^{(\hat{d}\hat{q})}\mathbf{T}_{(dq)} \begin{pmatrix} L'_{d,0} & L'_{dq,0} \\ L'_{dq,0} & L'_{q,0} \end{pmatrix} {}^{(dq)}\mathbf{T}_{(\hat{d}\hat{q})} \\ &= \begin{pmatrix} L'_{d,0} & L'_{dq,0} \\ L'_{dq,0} & L'_{q,0} \end{pmatrix} + \mathbf{R}(\alpha_6 + 6\gamma_{el}) \begin{pmatrix} \Delta L'_6 & 0 \\ 0 & -\Delta L'_6 \end{pmatrix} . \end{aligned} \tag{59}$$

Here, the left-hand side is the inductance matrix without a multiple saliency, which is rotated by the rotor position error. On the right-hand side, the inductance matrix with a multiple saliency is used. The estimation error is calculated by solving the system of equations, yielding

$$\gamma_{er} = -\frac{\text{atan}\left(\frac{L'_{dq,0}\sqrt{a} - \Delta L' L'_{dq,0} + \Delta L' \Delta L'_6 \sin(6\gamma_{el}+\alpha_6)}{\sqrt{\Delta L'^2 \cdot a} + {L'_{dq,0}}^2 - \Delta L'_6 L'_{dq,0} \sin(6\gamma_{el}+\alpha_6)}\right)}{2} \tag{60}$$

with

$$\begin{aligned} a = \Delta L'^2 - {\Delta L'_6}^2 \sin^2(6\gamma_{el} + \alpha_6) \\ + 2L'_{dq,0}\Delta L'_6 \sin(6\gamma_{el} + \alpha_6) \quad . \end{aligned} \tag{61}$$

In Fig. 14, this calculation is compared with the experimental result of the FIE-QD at a q-current of $i_{\hat{q}} = 10$ A.

The calculated and measured rotor position errors correlate closely. Since (60) is a complex term to be interpreted, a simplified case without mutual inductance ($L'_{\mathrm{dq},0} = 0$) is considered. This results in

$$\gamma_{\mathrm{er}} = -\frac{1}{2}\operatorname{atan}\left(\frac{\Delta L' \Delta L'_6 \sin\left(6\gamma_{\mathrm{el}} + \alpha_6\right)}{\sqrt{\Delta L'^4 - \Delta L'^2 \Delta L'^2_6 \sin^2\left(6\gamma_{\mathrm{el}} + \alpha_6\right)}}\right). \tag{62}$$

As long as the magnitude of the sixth harmonic of the inductance is significantly smaller than the difference between the self-inductances ($\Delta L'_6 \ll \Delta L'$), the equation can be approximated as

$$\gamma_{\mathrm{er}} \approx -\frac{1}{2}\operatorname{atan}\left(\frac{\Delta L'_6 \sin\left(6\gamma_{\mathrm{el}} + \alpha_6\right)}{\Delta L'}\right). \tag{63}$$

The form of this equation shows a correlation with the known error for a mutual inductance [e.g., (53)] in such a way that the maximum amplitude of the error decreases with an increasing difference between the self-inductances $\Delta L'$. The difference is that a sixth harmonic of the rotor position error is introduced.

B. Compensation of the Multiple Saliency

This error could be compensated by using the sixth harmonic in the derivation of the residual. But this would lead to a rather complicated term. Thus, the error is instead compensated using a linearization with an order of zero. For this purpose, the inductance matrix is evaluated using

$$\hat{\mathbf{L}}'_{(\mathrm{dq})} = \begin{pmatrix} L'_{\mathrm{d},0} & L'_{\mathrm{dq},0} \\ L'_{\mathrm{dq},0} & L'_{\mathrm{q},0} \end{pmatrix}\Bigg|_{i_{\hat{\mathrm{q}}}, i_{\hat{\mathrm{d}}}} + \Delta L'_6 \Bigg|_{i_{\hat{\mathrm{q}}}, i_{\hat{\mathrm{d}}}} \begin{pmatrix} \cos(6\gamma_{\mathrm{el}} + \alpha_6^*) & \sin(6\gamma_{\mathrm{el}} + \alpha_6^*) \\ \sin(6\gamma_{\mathrm{el}} + \alpha_6^*) & -\cos(6\gamma_{\mathrm{el}} + \alpha_6^*) \end{pmatrix}\Bigg|_{\hat{\gamma}_{\mathrm{el}}, i_{\hat{\mathrm{q}}}, i_{\hat{\mathrm{d}}}}. \tag{64}$$

The rotor position estimation, therefore, continues to work with the inductance matrix $\hat{\mathbf{L}}'_{(\mathrm{dq})}$ without a dependence on the rotor position within the numerical optimization, as this has already been evaluated. This approximation is valid as long as the change in rotor position during rotor position estimation is relatively small in relation to the sixth harmonic.

C. Experimental Results

Using the linearization of the inductance, the rotor position error over one electrical revolution is shown in Fig. 15.

Compared to the result without compensation of the sixth harmonic $\Delta L'_6$, the estimation error is greatly reduced. Again, an FFT is carried out to investigate different operating points. The results are shown in Fig. 16.

The comparison reveals that the sixth harmonic of the rotor position error is virtually eliminated. Only a rotor position error of the third and sixth harmonics remains at no-load operation. The magnitude of the sixth harmonic rotor position error is reduced by up to 2.8° in comparison to Fig. 12. Otherwise, only small changes of the second harmonic of the rotor position error arise.

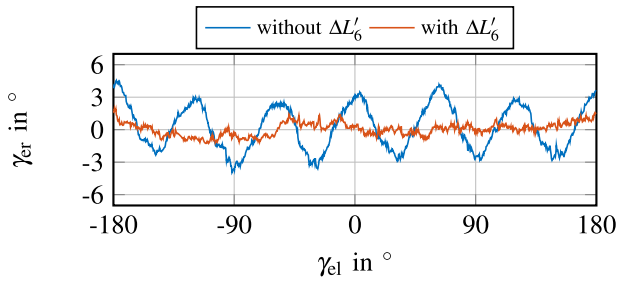

Fig. 15. Rotor position estimation error over an electrical period with and without compensation of the sixth harmonic at $n = 20\,^1/_{\mathrm{min}}$, $i_{\hat{\mathrm{q}}} = 10\mathrm{A}$, and $i_{\hat{\mathrm{d}}} = 0\mathrm{A}$.

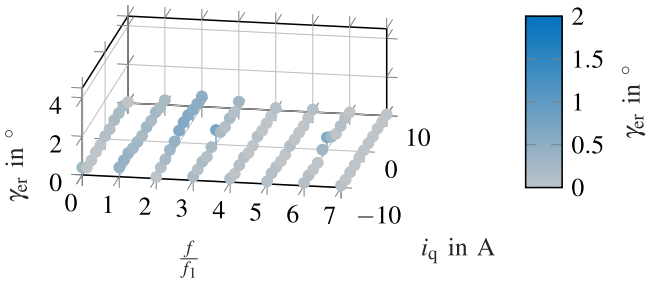

Fig. 16. Spectrum of the steady-state rotor position estimation error using the zeroth order approximation of the harmonic inductances at $n = 20\,^1/_{\mathrm{min}}$ and different q-currents.

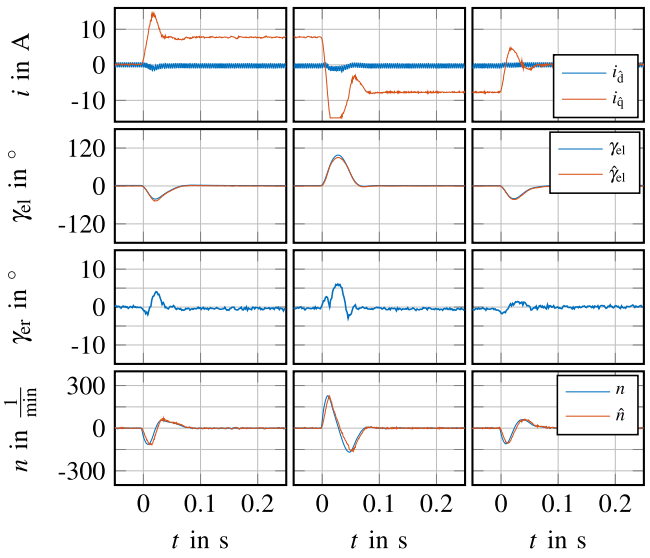

Fig. 17. Closed-loop SSC in position control with compensation of the mutual inductance via L'_{dq} and compensation of the sixth harmonic. Rated torque is applied (left), reversed (centre), and reduced to zero (right).

To test the compensation in transient operation, the position-controlled test scenario is repeated and shown in Fig. 17.

The figure shows that the harmonic error is reduced, leading to an overall reduction of the rotor position error in transient states in comparison to Fig. 11. Only a speed-dependent error remains, while the speed itself is falsely estimated. Thus, the compensation of the sixth harmonic is validated in this test case.

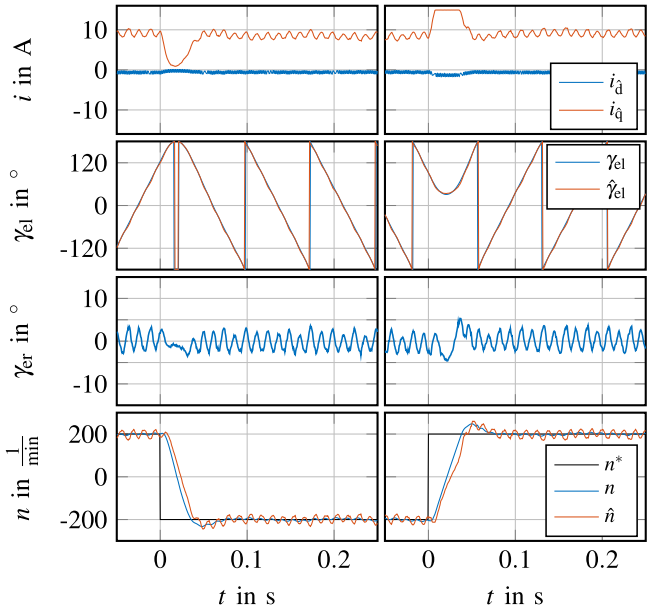

Fig. 18. Closed-loop SSC in speed control with compensation of the mutual inductance via L'_{dq} with speed setpoint step from $n^* = 200\ {}^1/_{\mathrm{min}}$ to $n^* = -200\ {}^1/_{\mathrm{min}}$ and back again.

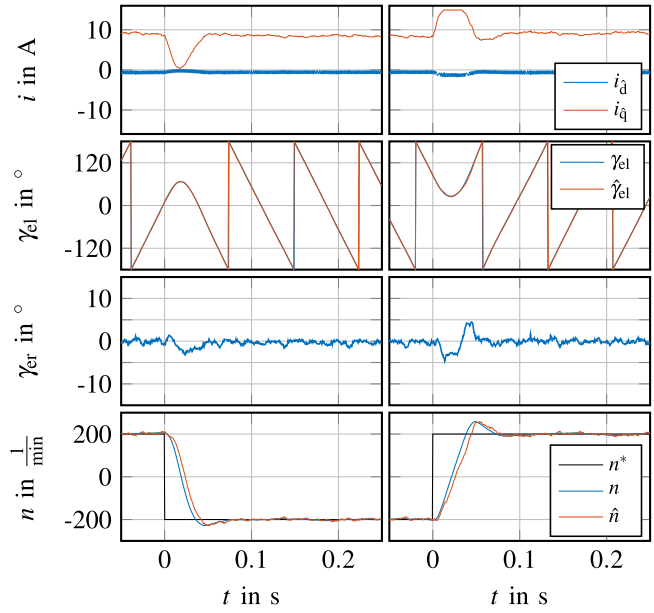

Fig. 19. Closed-loop SSC in speed control with compensation of the mutual inductance via L'_{dq} and compensation of the sixth harmonic with speed setpoint step from $n^* = 200\ {}^1/_{\mathrm{min}}$ to $n^* = -200\ {}^1/_{\mathrm{min}}$ and back again.

To further evaluate the functionality of the compensation, a different mode of operation is considered. The machine is speed controlled with a speed setpoint of $n^* = 200\ {}^1/_{\mathrm{min}}$, which is set to $n^* = -200\ {}^1/_{\mathrm{min}}$ and reversed back to $n^* = 200\ {}^1/_{\mathrm{min}}$. The result without the compensation of the sixth harmonic is shown in Fig. 18.

When the machine is operated at a steady speed, the sixth harmonic of the rotor position becomes apparent. In the transient states, this error is superimposed with the speed-dependent error, as long as the estimated speed deviates from the measured speed. The estimation error peaks in both transients slightly above $5°$. This result is repeated for the case with the compensation of the sixth harmonic in Fig. 19.

A comparison of the results shows the reduction in the sixth harmonic of the rotor position error. Again, a speed-dependent error remains. The estimation error during transients reaches slightly smaller values than it did without the compensation of the sixth harmonic. Overall, the compensation of the sixth harmonic of the inductances significantly reduces the sixth harmonic of the rotor position error. This is the main contribution of this work, when the experimental results are compared to the previous works [17], [18], [26]. Only in transient states does an error of more than $2.5°$ occur. The remaining error will form the subject of future work.

D. Parameter Sensitivity

For the compensation of the mutual inductance, a parameter sensitivity analysis is performed. The value of the sixth harmonic $\Delta L'_{6,\mathrm{est}}$ used in the estimator is varied and for the phase of the sixth harmonic an offset

$$\alpha_{6,\mathrm{est}} = \alpha_6^* + \alpha_{6,\mathrm{off}} \tag{65}$$

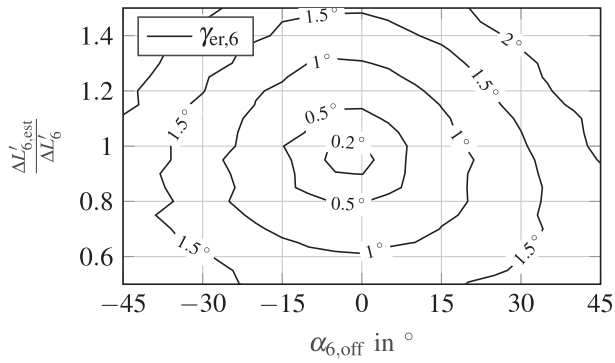

Fig. 20. Amplitude of the sixth harmonic of the estimation error $\gamma_{\mathrm{er},6}$ against different parameters for the compensation of the multiple saliency ($\Delta L'_6$ and $\alpha_{6,\mathrm{off}}$).

is added and varied. The result of the parameter variation for an operating point with $i_{\hat{\mathrm{q}}} = 10$ A is shown in Fig. 20. Here, the amplitude of the sixth harmonic of the estimation error $\gamma_{\mathrm{er},6}$ is plotted against different parameters for the compensation of the multiple saliency.

In the results of Fig. 20, one can see a reduction of the estimation error even if the amplitude and phase do not match the real values. Within the plotted parameter variation, the error of the sixth harmonic is always smaller than without compensation ($2.8°$).

E. Comparison With the State of the Art

In the following, the presented compensation is compared to the literature. The advantage of the presented compensation is that the effect has been analytically derived from the inductance

itself. For a changing operating point, the compensation has no transient response, since the parameter is directly read from a look-up table. As a disadvantage, the sixth harmonic of the inductances has to be known. Here, the inductance has been measured and thus the compensation is dependent on the quality of the measurement. The compensation according to [19] has the advantage of being independent of any previous measurements, but the compensation method introduces a transient response and relies on having a steady speed.

The approach of [16] also introduces no transient response. Still, a measurement using the measured rotor position is necessary to determine the compensation current of the harmonics. This leads to a similar result when compared to the presented approach of this article. In the future, investigations of a determination of the inductances using an electromagnetic simulation of the machine will be pursed. Through this, a measurement using the measured rotor position for the determination of the inductances may become obsolete. This reveals the benefit of using the inductance values, as the compensation can be achieved directly from calculated values.

VI. Conclusion

A method is proposed to reduce the constant and harmonic components of the estimation error introduced by machine saturation. By using the mutual inductance as additional information, the operation of SSC at highly saturated operating points is made possible. This is achieved by extending the residual employed to include the mutual inductance. In this way, the mutual inductance acts as an additional source of information, which is particularly valuable when the self-inductances reach similar values in the d- and q-axis, and makes the proposed SSC suitable for highly saturated machines.

Furthermore, the effects of higher order saliencies on the estimation error are analyzed and measures to compensate for these are presented. The proposed method is applied to the sixth harmonic of the estimation error. The parameters for the inductances have been obtained with an determination scheme based on the residual of the numerical optimization for SSC and using a position sensor. The experimental results show the effectiveness of the method in both transient and steady-state operation. In addition, a parameter sensitivity analysis is performed for the presented method, showing good performance even if parameter errors arise.

References

[1] M. J. Corley and R. D. Lorenz, "Rotor position and velocity estimation for a permanent magnet synchronous machine at standstill and high speeds," in *Conf. Rec. IEEE Industry Appl. Conf. 31st IAS Annu. Meeting*, 1996, pp. 36–41. [Online]. Available: https://ieeexplore.ieee.org/document/556994

[2] J. Holtz, "Sensorless control of induction machines—with or without signal injection?," *IEEE Trans. Ind. Electron.*, vol. 53, no. 1, pp. 7–30, Feb. 2006.

[3] O. Lehmann, J. Schuster, and J. Roth-Stielow, "Sensorless control techniques as redundancy for the control of permanent magnet synchronous machines in electric vehicles," in *Proc. IEEE Veh. Power Propulsion Conf.*, 2014, pp. 1–6.

[4] R. W. Hejny and R. D. Lorenz, "Evaluating the practical low-speed limits for Back-EMF tracking-based sensorless speed control using drive stiffness as a key metric," *IEEE Trans. Ind. Appl.*, vol. 47, no. 3, pp. 1337–1343, May/Jun. 2011.

[5] H. Kim and R. D. Lorenz, "Carrier signal injection based sensorless control methods for IPM synchronous machine drives," in *Conf. Rec. 39th IAS Annu. Meeting. IEEE Ind. Appl. Conf.*, 2004, pp. 977–984.

[6] S. Kim, J.-I. Ha, and S.-K. Sul, "PWM switching frequency signal injection sensorless method in IPMSM," *IEEE Trans. Ind. Appl.*, vol. 48, no. 5, pp. 1576–1587, Sep./Oct. 2012.

[7] D. Mingardi, M. Morandin, S. Bolognani, and N. Bianchi, "On the proprieties of the differential cross-saturation inductance in synchronous machines," *IEEE Trans. Ind. Appl.*, vol. 53, no. 2, pp. 991–1000, Mar. 2017.

[8] I. Hwang, Y.-C. Kwon, and S.-K. Sul, "Enhanced dynamic operation of heavily saturated IPMSM in signal-injection sensorless control with ancillary reference frame," *IEEE Trans. Power Electron.*, vol. 38, no. 5, pp. 5726–5741, May 2023.

[9] H. Sato, S. Aoyagi, H. Matsui, S. Taniguchi, and S. Ohara, "A development of short-time initial rotor position estimation technique based on the magnetic saturation and saliency," in *Proc. 25th Eur. Conf. Power Electron. Appl.*, 2023, pp. 1–8.

[10] M. Berto, L. Alberti, and S. Bolognani, "Experimental investigation on the self-sensing capability of synchronous machines for signal injection sensorless drives," in *Proc. IEEE Energy Convers. Congr. Expo.*, Oct. 2021, pp. 5078–5083.

[11] P. Guglielmi, M. Pastorelli, and A. Vagati, "Cross-saturation effects in IPM motors and related impact on sensorless control," *IEEE Trans. Ind. Appl.*, vol. 42, no. 6, pp. 1516–1522, Nov. 2006.

[12] P. Guglielmi, M. Pastorelli, and A. Vagati, "Impact of cross-saturation in sensorless control of transverse-laminated synchronous reluctance motors," *IEEE Trans. Ind. Electron.*, vol. 53, no. 2, pp. 429–439, Apr. 2006.

[13] Y. Li, Z. Q. Zhu, D. Howe, C. Bingham, and D. Stone, "Improved rotor position estimation by signal Injection in brushless AC motors, accounting for cross-coupling magnetic saturation," in *Proc. IEEE Ind. Appl. Annu. Meeting*, Oct. 2007, pp. 2357–2364.

[14] Y.-C. Kwon, J. Lee, and S.-K. Sul, "Extending operational limit of IPMSM in signal-injection sensorless control by manipulation of convergence point," *IEEE Trans. Ind. Appl.*, vol. 55, no. 2, pp. 1574–1586, Mar./Apr. 2019.

[15] J. Lee, Y.-C. Kwon, and S.-K. Sul, "Signal-injection sensorless control with tilted current reference for heavily saturated IPMSMs," *IEEE Trans. Power Electron.*, vol. 35, no. 11, pp. 12100–12109, Nov. 2020.

[16] Y.-C. Kwon, J. Lee, and S.-K. Sul, "Recent advances in sensorless drive of interior permanent-magnet motor based on pulsating signal injection," *IEEE Trans. Emerg. Sel. Topics Power Electron.*, vol. 9, no. 6, pp. 6577–6588, Dec. 2021.

[17] N. Himker and A. Mertens, "Using the flux increment over a pulse-width modulation period for anisotropy-based self-sensing control," in *Proc. 25th Eur. Conf. Power Electron. Appl.*, Sep. 2023, pp. 1–8.

[18] N. Himker, G. Lindemann, and A. Mertens, "Comparison of different compensation methods of the mutual inductance for self-sensing control," in *Proc. IEEE Int. Symp. Sensorless Control Elect. Drives*, Aug. 2023, pp. 1–8.

[19] M. Cizmic, A. Krämer, and A. Ali, "Machine-parameter-Independent reduction of harmonic errors in self-sensing control of PMSM," in *Proc. IEEE 10th Int. Symp. Sensorless Control Elect. Drives*, Sep. 2019, pp. 1–5.

[20] M. Seilmeier, S. Ebersberger, and B. Piepenbreier, "PMSM model for sensorless control considering saturation induced secondary saliencies," in *Proc. IEEE Int. Symp. Sensorless Control Elect. Drives Predictive Control Elect. Drives Power Electron.*, Oct. 2013, pp. 1–8.

[21] K. Burg, H. Haf, and F. Wille, *Höhere Mathematik für Ingenieure*, 8th ed. Berlin, Germany: Teubner, 2008.

[22] B. Weber, G. Lindemann, and A. Mertens, "Reduced observer for anisotropy-based position estimation of PM synchronous machines using current oversampling," in *Proc. IEEE Int. Symp. Sensorless Control Elect. Drives*, Sep. 2017, pp. 121–126.

[23] N. Himker, G. Lindemann, K. Wiedmann, B. Weber, and A. Mertens, "A family of adaptive position estimators for PMSM using the gradient descent method," *IEEE Trans. Emerg. Sel. Topics Power Electron.*, vol. 10, no. 2, pp. 1946–1962, Apr. 2022.

[24] N. Himker and A. Mertens, "Analytical design of self-sensing control for PMSM using quasi-direct calculation," *IEEE Open J. Ind. Appl.*, vol. 4, pp. 149–159, May 2023.

[25] N. Himker, M. Krümpelmann, and A. Mertens, "Low phase shift filter for current sensing based on the difference between AC machine models with and without iron losses," in *Proc. 24th Eur. Conf. Power Electron. Appl.*, Sep. 2022, pp. 1–10.
[26] N. Himker, M. Fehse, and A. Mertens, "Reducing the effect of iron losses on the quality of self-sensing control based on current oversampling," in *Proc. Int. Symp. Power Electron. Elect. Drives Autom. Motion*, Jun. 2024, pp. 837–843.
[27] B. Weber, T. Brandt, and A. Mertens, "Compensation of switching deadtime effects in voltage-fed PWM inverters using FPGA-based current oversampling," in *Proc. IEEE Appl. Power Electron. Conf. Expo.*, Mar. 2016, pp. 3172–3179.
[28] D. Diaz Reigosa, P. Garcia, D. Raca, F. Briz, and R. D. Lorenz, "Measurement and adaptive decoupling of cross-saturation effects and secondary saliencies in sensorless controlled IPM synchronous machines," *IEEE Trans. Ind. Appl.*, vol. 44, no. 6, pp. 1758–1767, Nov./Dec. 2008.

Niklas Himker (Member, IEEE) received the M.Sc. degree in electrical engineering in 2018 from Leibniz University Hannover, Hanover, Germany, where he has been working toward the Ph.D. degree in electrical engineering with the Institute for Drive Systems and Power Electronics since 2019.

His research interests include self-sensing control of electrical machines and FPGA-based estimation methods.

Pieris Sourkounis received the B.Sc. and M.Sc. degrees in mechatronics in 2020 and 2023, respectively, from Leibniz University Hannover, Hannover, Germany, where he has been working toward the Ph.D. degree in electrical engineering with the Institute for Drive Systems and Power Electronics since 2023.

His research interests include control of grid-connected converter system in power networks and self-sensing control of electrical machines.

Viktor Willich (Graduate Student Member, IEEE) received the B.Sc. degree in electrical engineering, information technology and business management in 2018 from Christian-Albrecht-University, Kiel, Germany, and the M.Sc. degree in electrical engineering in 2021 from Leibniz University Hannover, Hannover, Germany, where he is currently working toward the Ph.D. degree in electrical engineering with the Institute for Drive Systems and Power Electronics.

His research interests include self-sensing control of electric machines, parameter estimation, and signal processing.

Georg Lindemann received the M.Sc. degree in mechatronics and the Dr.-Ing. (Ph.D.) in electrical engineering from Leibniz University Hannover, Germany, in 2016 and 2024, respectively.

From 2014 to 2017, he was with Protolar GmbH and was involved in the development of power electronics prototypes. From 2017, he was a Research Associate with the Institute for Drive Systems and Power Electronics, Leibniz University Hannover. Since 2023, he has been with the CARIAD SE, Wolfsburg, Germany, as a Testinfrastructure Engineer.

Axel Mertens (Senior Member, IEEE) received the Dipl.-Ing. degree in electrical engineering and the Dr.-Ing. (Ph.D.) degree in electrical engineering from RWTH Aachen, Aachen, Germany, in 1992 and 1987, respectively.

In 1989, he was a Visiting Scholar with the University of Wisconsin at Madison, Madison, WI, USA. From 1993 to 2004, he was with Siemens AG, Erlangen and Nuremberg, Germany, with responsibilities for the control of large drives including a variety of converter topologies, and for a product range of medium voltage inverters. In 2004, he was a Professor for Power Electronics and Drives with Leibniz University Hannover, Hannover, Germany. He was the Department Chair of the Department of Electrical Engineering and Computer Science and as spokesman of the energy research center LiFE 2050 of Leibniz University Hannover. In addition to his academic duties, he had responsibilities within Fraunhofer IFAM, Bremen, and within Fraunhofer IEE in Kassel. He has authored or coauthored more than 200 scientific papers. His research interests include the application of power semiconductor devices, design of power electronic circuits and systems, and control of power converters and drives, contributing to automotive and energy applications, as well as industrial drives. Outstanding research contributions include applications of WBG devices in e-mobility, control and topologies of modular multilevel converters, condition monitoring of power electronic devices, and highly dynamic self-sensing control of electric machines.

Dr. Mertens was a Chairman of IEEE Joint IAS/PELS/IES German Chapter and an Associate Editor for IEEE TRANSACTIONS ON POWER ELECTRONICS. Since 2019, he has been a member of the PELS AdCom. He was the Chairman of EPE'22 ECCE Europe in Hannover.